Constitutive response predictions of both dense and loose soils with a discrete element model

Luc Sibille, Nadia Benahmed, Félix Darve

Constitutive response predictions of both dense and loose soils with a discrete element model

Luc Sibille[a,*], Nadia Benahmed[b], Félix Darve[a]

[a] *Univ. Grenoble Alpes, CNRS, Grenoble INP, 3SR, F-38000 Grenoble, France*
[b] *INRAE, Aix Marseille Univ, Research Unit Recover, 13182 Aix-en-Provence cedex 5, France*

Abstract

The capability of a discrete element model to predict the constitutive response of a soil is investigated in this paper. The discrete model is constituted of spherical particles with a contact law embedding inter-particle rolling resistance. The study has been carried out in a constrained framework: the complexity of the model is limited in favour of its simplicity of use, the model calibration is independent of the initial state of the soil, the validation of the model has to be robust in the sense that validation loading paths should differ strongly from the calibration loading paths. To reach these objectives, the contact law of the model was slightly enriched with the implementation of a non-constant friction angle, and both porosity and connectivity are controlled for the numerical simulation of the initial soil state. Numerical predictions of the model on the validation loading paths show that such a modelling framework, associating the model itself and the preparation methodology of the numerical sample, leads to good qualitative and quantitative predictions. This is the case in particular for non-rectilinear loading paths or loading paths involving rotation of principal stress axes, while the model is calibrated from monotonous drained triaxial compressions only.

Keywords: Discrete-element modelling, constitutive soil behaviour, triaxial tests.

*Corresponding author
Email address: luc.sibille@3sr-grenoble.fr (Luc Sibille)

1. Introduction

The discrete element method (DEM; Cundall and Strack, 1979) can be used to investigate and characterize the physics taking place at the scale of particles in granular soils and granular materials (e.g. Rajaï et al., 1998; Iwashita and Oda, 2000). Nevertheless, DEM has been also largely implemented as a constitutive model to simulate and investigate the constitutive behaviour of soils at the scale of the representative elementary volume, often from a qualitative point of view (see for instance Bardet, 1994; Sibille et al., 2015). Furthermore, constitutive responses of soils at macroscopic scale can be predicted with the DEM, as soon as the shape of the particles is either described explicitly in the model (Kawamoto et al., 2018; Lee et al., 2012), or indirectly via enriched contact laws (Belheine et al., 2009; Widulinski et al., 2009). Models explicitly describing the shape of the particles are very promising regarding their ability to describe the constitutive response of granular soils as sand (Karapiperis et al., 2020) or ballast (Quezada et al., 2014). In addition, recent advances as the level set DEM (LS-DEM) offer the possibility to consider faithful reproductions of real soil grains (Kawamoto et al., 2018). However, such an approach holds for granular soils, whereas many natural soils are not only granular and include finer elements as silt and clay. Besides, the DEM computation cost increases rapidly, on one hand with the quality of the description of the shape of the particles, and on the other hand with the number of particles. An insight about the number of particles required to constitute a representative elementary volume for increasing uniformity coefficient can be found in Shire et al. (2014). Consequently, the computational cost related to the explicit description of particles become prohibitive in the case of well graded soils (with a relatively high uniformity coefficient), or when boundary value problems (and not only representative elementary volumes) are considered. Alternatively, the implementation of spherical particles with enriched contact laws to overcome the oversimplified representation of particle shapes consists somehow in intro-

ducing some phenomenological ingredients in the DEM. This can be seen as a drawback, losing the direct physical representation of soil particles and the accurate description of the local physics. However, such a discretization of soil with spherical elements (or clumps of few spheres) and ad hoc contact laws stays today an efficient alternative way to describe natural soils (Villard and Chareyre, 2004) and to tackle engineering problems (Li et al., 2019; Hassan and El Shamy, 2019; Villard et al., 2016) with a limited computational cost. It is worth mentioning that phenomenological constitutive relations implemented in finite element or finite difference methods constitute very efficient ways, among others with respect to the computational cost, to address boundary value problems. However conventional elastoplastic constitutive relations (typically with one or two plastic potentials) do not lead to realistic predictions for some loading paths, for instance with rotation of principal stress axes or cyclic paths (Saada and Bianchini, 1988) (or require a specific formulation and calibration in the latter case) and in the post-failure regime (Daouadji et al., 2011).

This paper focuses on the ability of a discrete element model to predict the constitutive response of a soil at the macroscopic scale. In this objective, a discrete model constituted of spherical particles is considered with a rolling resistance at inter-particle contacts to mimic the effect of the shape of real particles (angular or anisotropic) (Oda and Iwashita, 2000). Rorato et al. (2021) shown that the average rotation of the grains in sands can be correctly described by embedding rolling resistance in DEM. Such a model also presents the advantage of a limited computational cost and remain relatively general (i.e. usable for granular soils and for soils with a wide grain size distribution or including fines). Its prediction ability at the macroscopic scale in the case of dense granular soils is rather satisfying, although some refinement can still be investigated in order to better adjust the stiffness in the hardening regime when the material is sheared, or to take into account the dependency of the internal friction angle on the mean pressure (Plassiard et al., 2009; Sibille et al., 2019).

However, the prediction of DEM in the case of loose soils may be far from satisfactory (Aboul Hosn et al., 2017). An illustration of such a weak prediction

ability for an initial loose state is given in Figure 1. The discrete model, made of spherical particles with contact rolling resistance, was calibrated on a dense Hostun sand with a relative density, D_r, close to 1 (see the calibration curves from drained triaxial compressions further in this paper in Figure 7, and details of the calibration are given in Sibille et al., 2019). Responses simulated with the model are compared in Figure 1 with experimental results for an initially loose Hostun sand ($D_r \approx 0.1$) and for three different loading paths: a drained compression, an undrained compression, and a drained compression followed by a constant stress deviator path (q-constant path). The following drawbacks are observed: the shear strength is overestimated in drained condition and largely underestimated in undrained condition (with a precipitate collapse of the numerical sample), the dilatancy along the q-constant path is not reproduced (as it was also shown in Aboul Hosn et al., 2017).

Finally, many studies based on a DEM model embedding inter-particle rolling resistance investigated the constitutive response of soils (see among others: Gu et al., 2020; Jiang et al., 2019; Martin et al., 2020). However, few of them assess the numerical model with respect to different initial densities of the considered soil (Gu et al., 2020) and validation of the calibrated model with blind predictions of experimental soil response remains poorly developed.

Consequently, the aim of this paper is to present a discrete numerical model with a good quantitative prediction ability of the mechanical behavior of initially both dense and loose soils with a relative density ranging from 10% to 100%. The main enrichment of the discrete model concerns, on one hand the contact law which has been slightly improved in order to describe a non-constant internal friction angle at the macroscopic scale; on the other hand, a particular sample preparation methodology in order to control both the porosity and the connectivity of the granular assembly at the initial state. It is also important to keep in mind the constraints which have been fixed for this study:

- the definition of the model and the preparation of the granular initial state

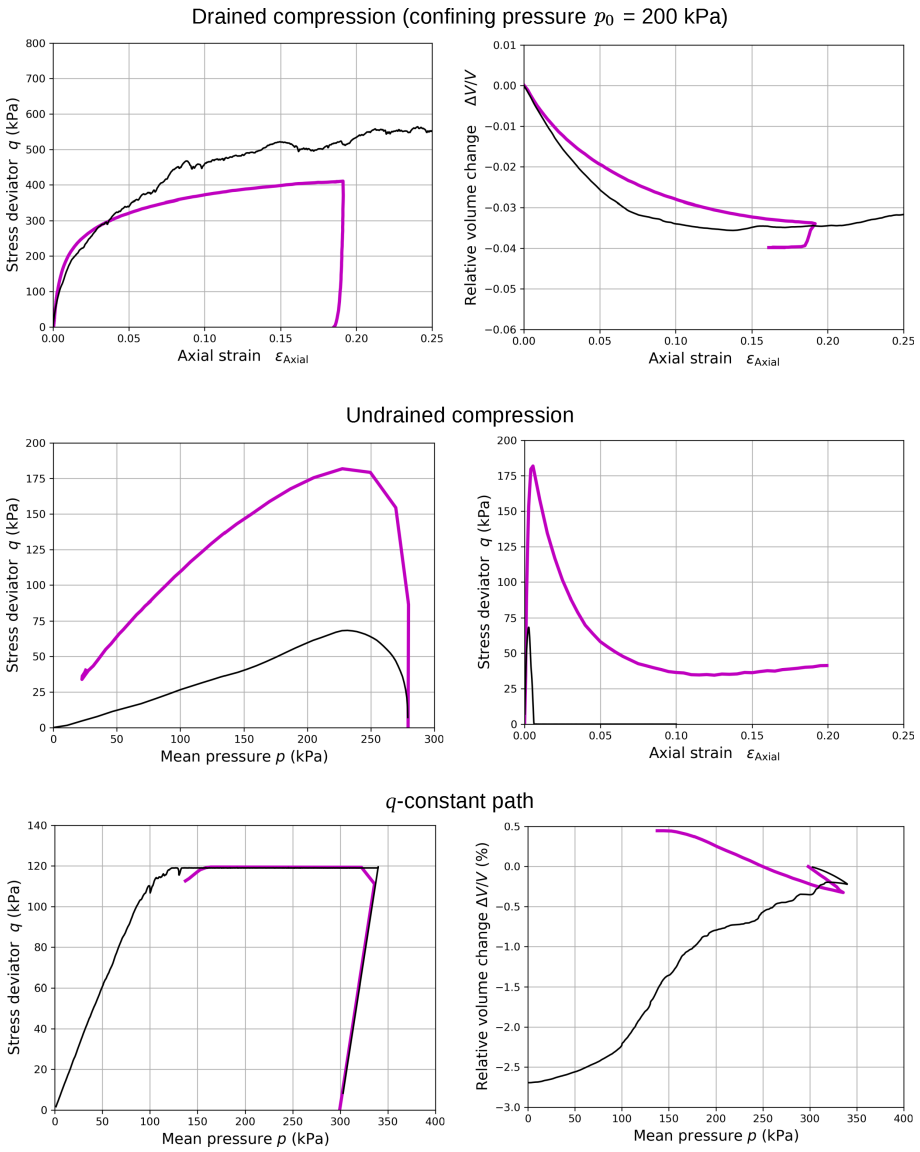

Figure 1: Simulation of the response of the loose Hostun sand with a discrete numerical model proposed in Sibille et al. (2019) and calibrated on dense Hostun sand: the simulated response (thin black line) is compared to experimental results (thick magenta line) for a drained compression (test TMRF5 from Benahmed, 2001), an undrained compression (test 8ND from Bousquet et al., 1994), and a constant stress deviator path (test CSD1 from Daouadji et al., 2011).

should stay relatively simple to make possible the implementation of such a model to study a boundary value problem in an engineering context;

- the calibration of the mechanical parameters of the model should be independent of the initial density state (as the mechanical contact properties of two sand grains are independent of the bulk density);

- the model has to be rigorously validated by testing loading paths for the validation step strongly different from the loading paths used for the calibration.

The discrete element model used for this study, and in particular the inter-granular contact laws, are defined in a first part of the paper. Then, the Hostun sand "RF", used here as the reference soil, is presented together with the origin of experimental data of mechanical tests performed on this sand, and coming from the literature or experimental databases. The experimental results, constituting an important base for this study, present the particularity to concern always the same Hostun sand, but to come from different authors (and thus different operators) and from different kinds of testing devices. In a third section, the methodology to generate the numerical granular samples and to control their initial states is discussed, followed by the presentation of the calibration process of the model. The resulting calibration on the Hostun sand is eventually displayed. The next section is devoted to the definition of the loading paths considered for the validation of the model. Prediction capability of the model is assessed by comparing the simulated constitutive responses to the responses measured experimentally on these loading paths. Finally, main findings and conclusions are discussed in a last section.

2. The discrete element model

The discrete element model is constituted of spherical particles. It involves an inter-granular contact law with a rolling moment acting against the relative

rotation of the particles in contact, in addition to the more classical Coulombian friction model. This model has already been defined in Aboul Hosn et al. (2017) and Sibille et al. (2019) and the rolling resistance at contact has been shown as a relevant and simple way to describe and predict accurately the shear strength in drained conditions for a given mean pressure. This model includes a constant contact friction angle resulting, at the macroscopic scale, in a constant internal friction angle. However, the failure surface for real soils may be slightly non-linear with respect to the mean pressure, with possibly a relatively strong increase of the internal friction angle when the mean pressure lowers. This is observed for granular soil (Lancelot et al., 2006; Maksimovic, 1989), rockfill (Barton and Kjaernsli, 1981) and glass beads (Hazzar et al., 2020) and might result from the alteration of grain surface properties with the confining pressure (Barton and Kjaernsli, 1981), but it has also been reported for a compact clay at very low mean pressure (Maksimovic, 1989).

Since undrained compressions and q-constant paths induce strong reductions of the mean effective pressure, the underestimation by the model of the shear strength in undrained conditions, or the non reproduction of a dilatative response along a q-constant path (as shown in Figure 1) may be attributed to a failure surface of the Mohr-Coulomb type (i.e. with a constant internal –macroscopic– friction angle).

Besides, the contact friction coefficient between two bodies is known from tribology to possibly depends on the normal contact force, even if this dependence may be quite weak for some ranges of normal forces (Popova and Popov, 2015; Popov, 2017). Therefore, the contact law presented here after is enriched with a non-constant contact friction coefficient, depending on the normal contact stress as suggested previously by Suhr and Six (2017).

Let's consider a couple of interacting particles as displayed in Figure 2a with an overlap δ_n and a normal $\vec{n}$ to the tangent contact plane. Then the normal

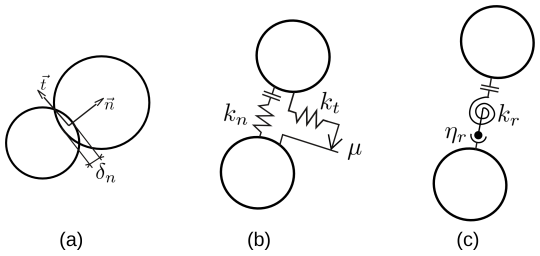

Figure 2: Contact between two particles: overlap (a) and rheological models of the contact law with sliding friction (b) and rolling resistance (rolling friction) (c).

and tangential contact forces write respectively (Figure 2b):

$$\vec{F_n} = k_n \, \delta_n \, \vec{n} \tag{1}$$

$$\Delta\vec{F_t} = -k_t \, \Delta\vec{u}_t \tag{2}$$

where k_n and k_t are normal and tangential stiffnesses considered constant. $\vec{F_t}$ is computed incrementally from the relative tangential displacement $\vec{u}_t$ at the contact due to the non-linearity introduced by the dry friction. The latter implies that:

$$||\vec{F_t}|| \leq \mu \, ||\vec{F_n}|| \tag{3}$$

with μ the contact friction coefficient.

μ is either chosen constant (in the phases of generation of the numerical sample) or defined as a function of the normal contact stress σ_c (Darve and Dendani, 1988; Maksimovic, 1989):

$$\mu = \mu_{\min} + \frac{\mu_{\max} - \mu_{\min}}{\sigma_c/\sigma_c^R + 1} \tag{4}$$

Then $\mu_{\min}$ and $\mu_{\max}$ constitute two parameters of the contact law. For a nil normal contact stress (i.e. a nil normal contact force) $\mu = \mu_{\max}$, while for an increasing contact stress the friction coefficient decreases to tend asymptotically to $\mu_{\min}$.

σ_c^R is a reference contact stress chosen arbitrarily as the mean normal contact stress that would occur in an idealized isotropic granular assembly subjected to a reference isotropic confining stress of 100 kPa. Assuming a granular medium of porosity 0.4, a rough estimation of σ_c^R is then given thanks to the mixture theory by $100/(1-0.4) \approx 167$ kPa.

σ_c is deduced for each contact from the normal contact force with:

$$\sigma_c = \frac{||\vec{F}_n||}{\pi\, R_{\text{mean}}^2} \tag{5}$$

where R_{mean} is the harmonic mean of the radii R_1 and R_2 of the two spheres involved in the contact:

$$R_{\text{mean}} = 2\frac{R_1\, R_2}{R_1 + R_2} \tag{6}$$

Figure 3 gives an example of the change of the contact friction coefficient with the normal contact stress for the parameters calibrated further in this paper ($\mu_{\min} = 0.35$ and $\mu_{\max} = 1.22$). The contact friction coefficient increases importantly for low normalized contact stress, which is drawing a parallel with the strong increase of the internal friction angle found at low confining pressure for the dense Hostun sand (up to 48 to 49 degrees for the dense Hostun sand under a confining pressure of 20 kPa (Lancelot et al., 2006)). Interestingly, the relation 4, inspired from the phenomenological constitutive relation developed by Darve and co-authors for soils (Darve and Dendani, 1988; Darve et al., 1995), can be seen as a simplified expression of the normal stress-dependent coefficient of friction implemented by Suhr and Six (2017) and deduced from the friction model of a wheel-rail (steel-steel) contact.

Concerning the inter-particle rolling resistance, the rolling moment at contact, $\vec{M}_r$, is defined from a constant rolling stiffness k_r and acts against the relative rolling rotation of the particles $\vec{\theta}_r$ (Figure 2c):

$$\Delta\vec{M}_r = -k_r\, \Delta\vec{\theta}_r \tag{7}$$

It is limited by a plastic threshold (rolling friction) expressed as:

$$||\vec{M}_r|| \leq ||\vec{F}_n||\, \eta_r\, \min(R_1, R_2) \tag{8}$$

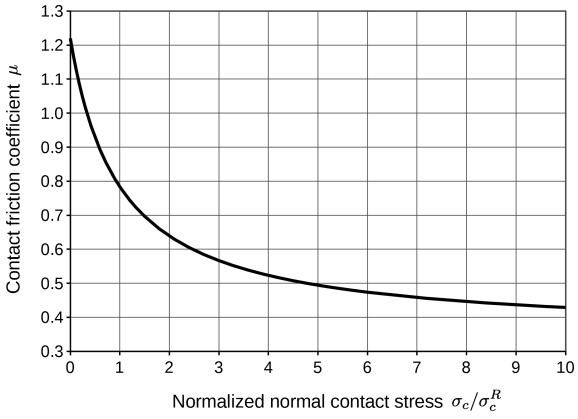

Figure 3: Dependence of the contact friction coefficient on the normal contact stress for $\mu_{\min} = 0.35$ and $\mu_{\max} = 1.22$.

where η_r is the rolling friction coefficient.

Finally, contact stiffnesses are defined from a stiffness modulus E_c and dimensionless tangential and rolling coefficients, α_t and α_r respectively:

$$k_n = E_c\, R_{\text{mean}}; \qquad k_t = \alpha_t\, k_n; \qquad k_r = \alpha_r\, R_1\, R_2\, k_t \tag{9}$$

Consequently, to describe a non-cohesive soil, the numerical model requires a total of six mechanical parameters: 3 elastic parameters (E_c, α_t, α_r) and 3 friction coefficients ($\mu_{\min}$, $\mu_{\max}$, η_r).

Moreover, inter-particle adhesion may be used during the sample preparation as a way to influence the connectivity of the granular assembly to produce different initial micro-structures. Therefore, adhesive normal and tangential contact forces, F_n^A and F_s^A, are defined from an adhesive stress σ_A such that:

$$F_n^A = F_t^A = \sigma_A\ [\min(R_1, R_2)]^2 \tag{10}$$

Then, the contact presents a resistance to a tensile normal force as long as:

$$\vec{F}_n\,.\,\vec{n} > -F_n^A\,, \tag{11}$$

and the shear force is limited by:

$$||\vec{F}_t|| \leq \mu\,(\vec{F}_n\,.\,\vec{n}) + F_t^A. \tag{12}$$

Constitutive simulations presented in this paper were performed thanks to the open-source code YADE (Smilauer, 2015), from a parallelepipedic cell with periodic limit conditions and including 10 000 particles.

The computational time for a simulation as the ones presented here after is typically of few hours on a conventional desktop computer ($\approx$ 2 to 4 hours on a single 2.5 GHz processor, except for cyclic liquefaction tests). Hence, much complex simulation domains, as boundary value problems, can be tackled in a reasonable time with parallel computations on a recent computing workstation.

3. Experimental data on Hostun sand "RF"

Calibration and validation of the numerical model are performed from triaxial loadings performed on the Hostun sand "RF". This sand is chosen as the reference soil for this study because a large series of experimental results is available coming from different operators using different loading devices, with a wide variety of loading paths (including non axisymetric stress states and rotation of principal stress axises). A description of Hostun sand is given by Flavigny et al. (1990). It is composed of sub-angular to angular grains with a uniform grain size distribution as shown in Figure 4 (uniformity coefficient $C_U = 1.8$) and a mean grain size $D_{50} = 0.35$ mm. Depending on the technique used, the minimum void ratio was found in the range $e_{\min} \in [0.624;\ 0.648]$ and the maximum void ratio in the range $e_{\max} \in [0.961;\ 1.041]$.

Two sets of experimental tests are considered in this paper. A first set of tests were performed on dense samples with a relative density D_{r} after consolidation close to 1.0 using a true triaxial apparatus by Zitouni (1988) and Lanier and Zitouni (1988). This apparatus consists in a parallelepipedic box made of six rigid steel platens. The latter can move in such a way that the inside box deforms

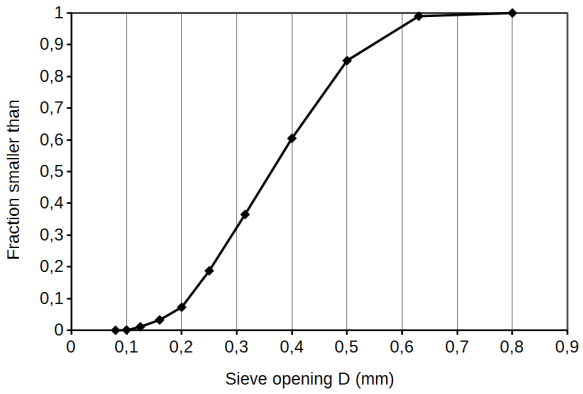

Figure 4: Grain size distribution of the Hostun sand "RF", after Flavigny et al. (1990).

by staying parallelepipedic. By this way, the three principal components of stresses or strains can be controlled independently by controlling the kinematic of the platens: either directly for strains by adjusting the platen displacements, or indirectly for stresses thanks to a closed-loop control. The second set of tests were performed on loose samples with $D_{\mathrm{r}} \approx 0.1$ after consolidation and using conventional axisymmetric triaxial cells. Data was collected from Benahmed (2001) and Daouadji et al. (2011), and from a database compiling the triaxial tests performed at "laboratoire 3SR" (Grenoble, France) on Hostun sand RF (Bousquet et al., 1994).

It is worth noting some major differences between the two sets of tests. Dense sand samples were created by dry tamping whereas the moist tamping technique was applied to get loose samples. The loose samples were saturated before triaxial compressions whereas dense samples were kept dry. Finally, the initial cylindrical shape of loose samples, enclosed into a rubber membrane, may change into a barrel shape during the compression, while the dense samples kept at any time a parallelepipedic shape as imposed by the rigid platens.

4. Sample generation and identification of the mechanical parameters

4.1. Control of the initial state

The initial state of the numerical granular assembly constitutes a key point to reach quantitative prediction of soil responses (Combe and Roux, 2011). When the numerical sample is sheared, the volumetric deformation and the peak shear strength depend strongly on its initial density, as for real soils. Moreover, the stiffness in the hardening regime is influenced by the initial connectivity of the granular assembly (Roux and Combe, 2010). Therefore, a preparation methodology of the granular assembly is presented in this section in such a way that the initial density of the packing and its initial connectivity can be controlled independently.

The input parameters of this preparation methodology are a target porosity n_t, an inter-particle adhesion σ_A, and the confining pressure p_0 desired at the end of the compaction. The porosity reached at the end of the process depends mainly on the input target porosity, while the coordination number of the packing is influenced by the inter-particle adhesion. The preparation process is constituted of three steps.

1. Strain controlled isotropic compression of a cloud of non-overlapping particles with a nil inter-particle friction ($\mu = 0$) and a fixed inter-particle adhesion σ_A until reaching the target porosity n_t. During this step the mean pressure in the sample can become higher than p_0.
2. Progressive reduction of the inter-particle adhesion while the volume of the sample is fixed (density is kept constant) until reaching either a nil adhesion ($\sigma_A = 0$), or a mean pressure equal to the desired confining pressure p_0 (as the mean pressure decreases with the reduction of the inter-particle adhesion).
3. Adhesion is set to zero ($\sigma_A = 0$, if a nil adhesion has not been reached in the previous step) and the inter-particle friction is set to its nominal value (i.e. the value chosen to simulate the constitutive soil behaviour). Then a stress controlled isotropic compression is performed until the stabilization

of the numerical sample under the desired isotropic confining pressure p_0. During this last step, the porosity of the sample may evolve slightly (with respect to n_t fixed at step 1) until reaching, at equilibrium, an initial porosity n_0 (i.e. the initial porosity that will be considered for the consecutive mechanical loadings). In other words, the operator has to choose n_t in step 1 by estimating a priori the possible shift from n_t to n_0.

At the end of the third step the granular assembly reaches an initial state characterized by the isotropic confining pressure p_0, a porosity n_0, and a connectivity assessed via the coordination number z_0 (the mean number of contacts per particles) or the mechanical coordination number $z_{0\mathrm{m}}$, as defined by Thornton (2000), where only particles involved in two or more contacts are taken into account (particles not contributing to the stability of the packing are discarded).

Figure 5 presents an illustration of the coordination number reached for initially dense ($n_0 = 0.36$) and loose ($n_0 = 0.41$) granular assemblies under a confinement $p_0 = 300$ kPa, with respect to the adhesion σ_A set at the beginning of the process. Note that low adhesion values are not considered for the loose case because a sufficiently high adhesion is necessary to promote loose initial states. Hence, if a high target porosity in combination with a low adhesion are chosen for the generation methodology, a rather unstable configuration will be generated during steps 2 and 3 and the porosity will converge toward a low value n_0 during the step 3 (stabilisation phase).

Generally speaking, opposite trends are observed with respect to n_0. In the dense case, inter-particle adhesion promotes the creation and the preservation of contacts during the generation process and connectivity increases with the adhesion. In the loose case, inter-particle adhesion promotes stable open microstructure when high target porosity are chosen and the connectivity decreases with adhesion. Moreover, a relatively wide range of coordination numbers is accessible in the dense case, whereas this range is much reduced in the loose case. In the latter case, it is difficult to keep a stable packing when the coordination

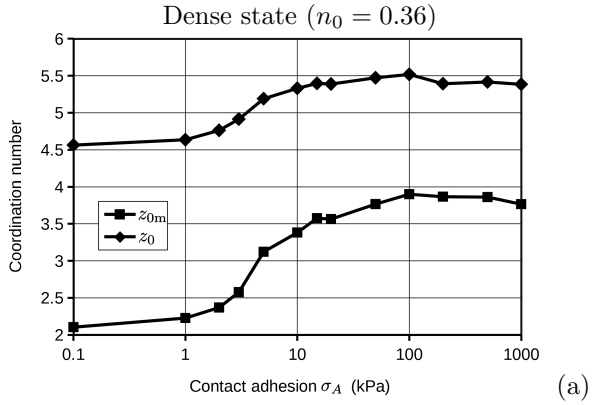

Figure 5: Dependence of the coordination number z_0 and mechanical coordination number $z_{0\mathrm{m}}$ on the adhesion σ_A chosen for the compaction phase; the porosity is fixed at $n_0 = 0.36$ for the dense state and $n_0 = 0.41$ for the loose state.

number is decreased (by choosing high adhesion); besides, high connectivities cannot be reached in combination with a high porosity.

Finally, let's recall that the objective is to simulate a micro-structure made of spherical particles that would result in a macroscopic constitutive response similar to the one of a soil composed of non-spherical particles. Consequently, adhesion values, considered for instance in Figure 5, are not necessarily representative of the capillary pressures in a partially saturated soil as the numerical micro-structure is not a direct reproduction of the real one.

4.2. Calibration methodology

As indicated in the introduction, one of the objectives of this paper is to identify the mechanical parameters of the model is such a way the parameters are identical for initially dense and loose soils. The residual shear strength at large deformations (critical shear strength) is one of the important soil characteristics used to calibrate the model. However, the mobilized friction angle observed at large deformations from drained triaxial compression tests may be different for initially dense and loose states (Tatsuoka et al., 1986; Wu, 1990; Chu, 1995). Figure 6 presents such results in the case of the Hostun sand (Benahmed, 2001). For initially loose states (initial relative density $D_{\mathrm{r}}^{\mathrm{i}} = 0$), the mobilized friction angle can be more than 3 degrees lower than the one at a medium dense state ($D_{\mathrm{r}}^{\mathrm{i}} = 0.5$). A greater gap is even reached if again denser initial states are considered. This difference is mainly attributed to the limited axial deformation (due to technical constraints) that can be imposed with a conventional triaxial device (typically about 20 %). For relatively dense Hostun sands, the final state reached at the end of the compression is usually still in the softening regime and is not a steady state in terms of volumetric deformation and mobilized friction angle. The critical state should stand beyond the last state observed experimentally. Therefore, the residual shear strength observed

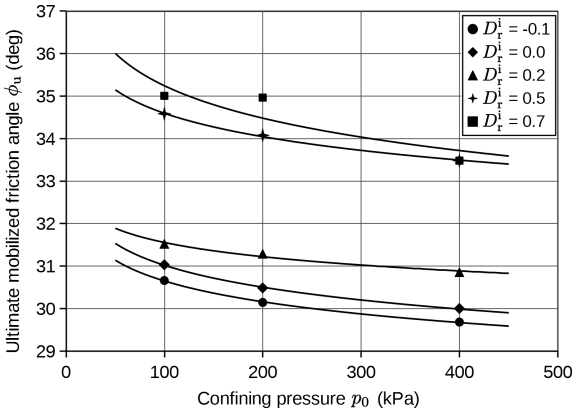

Figure 6: Mobilized friction angle measured at the end of drained compressions on Hostun sand for different initial densities, after Benahmed (2001).

from a loose initial state will be preferred for the calibration of the model, since it is obtained for a lower deformation of the sample more easily achieved with a triaxial device.

From a numerical point of view, the peak shear strength of an initially dense specimen strongly depends on the contact friction coefficient. Consequently, the calibration of the contact friction coefficient requires compression tests on initially dense samples. Furthermore, if the contact friction coefficient μ is assumed dependent on the normal contact stress (as in Equation 4), then several drained compressions on initially dense states with different confining pressures should be used for the calibration (if μ is assumed constant then a single compression from a dense state is enough, see Sibille et al., 2019).

By taking into account the above considerations, the calibration of the model requires at least one drained compression on the loose sand and several drained compressions (ideally 3) on the dense sand. Then, the following calibration methodology is proposed. It considers a non-constant contact friction coefficient, but for sake of simplicity the latter is fixed as constant in the first steps of the process.

1. Numerically the shear strength at large deformation depends only on the rolling friction coefficient η_r and not on the initial density, nor the contact friction coefficient if μ is not too low (Aboul Hosn et al., 2017) and fixed arbitrarily here to a constant value, as 0.5 for instance. Consequently, η_r is the first parameter of the model being calibrated to fit the residual shear strength identified from a drained compression performed on the initially loose sand.
2. The initial density is the first factor influencing the volumetric deformation (dilatancy/contractancy) and the peak shear strength. Therefore, the initial density is tuned in order to approach as close as possible both the volumetric deformation and the peak shear strength obtained from a

drained compression on the dense sand with a given confining pressure. During this phase μ is still kept constant. Besides, the contact adhesion involved in the sample generation is fixed in this step to a default value (relatively low for a dense sample), since the initial coordination number and the necessary adhesion to reach it will be identified latter.

3. Once the initial density for the dense case has been identified, the contact friction coefficient is calibrated to improve the reproduction of the volumetric deformation and the peak shear strength. In a first time, μ is calibrated as a constant parameter from the single compression on the dense sand considered in step 2. Then, the dependence of μ with the contact normal stress (Eq. 4) is switched on to identified $\mu_{\min}$ and $\mu_{\max}$ from compressions at different confining pressures (but ideally identical initial densities).
4. The initial coordination number for the dense state is tuned according to the sample generation detailed in previous section in order to fit the stress-strain response of the dense sand in the hardening regime. As initial density, contact friction coefficient and initial coordination number may have cross effects on volumetric deformation, peak shear strength and stiffness in the hardening regime, it may be useful to loop over steps 2 to 4 to converge towards the most suitable set of parameters.
5. Finally, initial density and coordination number are searched (always according to the process defined in previous section) to fit respectively the volumetric deformation and the stiffness in the hardening regime for the initial loose state, or even any initial state different from the dense state considered previously.

The choice of the elastic parameters are not discussed here. But if they are sufficiently close to the rigid grain limit (Roux and Combe, 2010; Roux and Chevoir, 2005), then the plastic properties of the granular assembly at the macroscopic scale depend on the contact plastic parameters (η_r, $\mu_{\min}$, $\mu_{\max}$) only (Aboul Hosn et al., 2017). Besides, the stiffness of the numerical sample

Table 1: Properties of the discrete model identified from the calibration on initially loose and dense Hostun sand RF.

	Initial state			**Mechanical parameters**					
	n_0	z_0	$z_{0\mathrm{m}}$	E_c (MPa)	α_t	α_r	$\mu_{\min}$	$\mu_{\max}$	η_r
Dense ($p_0 = 350$ kPa)	0.369	4.33	1.90	500	0.30	5.00	0.35	1.22	0.25
Loose ($p_0 = 300$ kPa)	0.444	4.17	2.73						

at low deformation depends on the elastic contact parameters but also on the initial density and connectivity. For this paper, elastic contact parameters where chosen a priori sufficiently high to approach the rigid grain limit and they have not been calibrated. Global stiffness at low deformation was found satisfying after identifying the initial porosity and connectivity.

4.3. Calibration on Hostun sand

The particle size distribution considered in the numerical model is identical to the one of Hostun sand RF shown in Figure 4, except the extreme parts of the distribution where particles smaller than 0.125 mm and larger than 0.63 mm (representing 2% of the total mass of particles) have been discarded. The mechanical parameters resulting from the calibration on the Hostun sand RF are given in Table 1, together with the properties of the initial states of the model. The calibration curves are shown in Figure 7 for the dense Hostun sand and in Figure 8 for the loose sand. In these figures, as for the following ones, experimental results are presented with a thick magenta lines (or thick grey in black and white printings) and simulated responses are plotted with thinner black lines.

Concerning the dense sand, three axisymmetric drained compressions at confining pressures $p_0 = 200$, 350 and 500 kPa respectively have been considered for the calibration (i.e. the following condition is imposed to the true triaxial

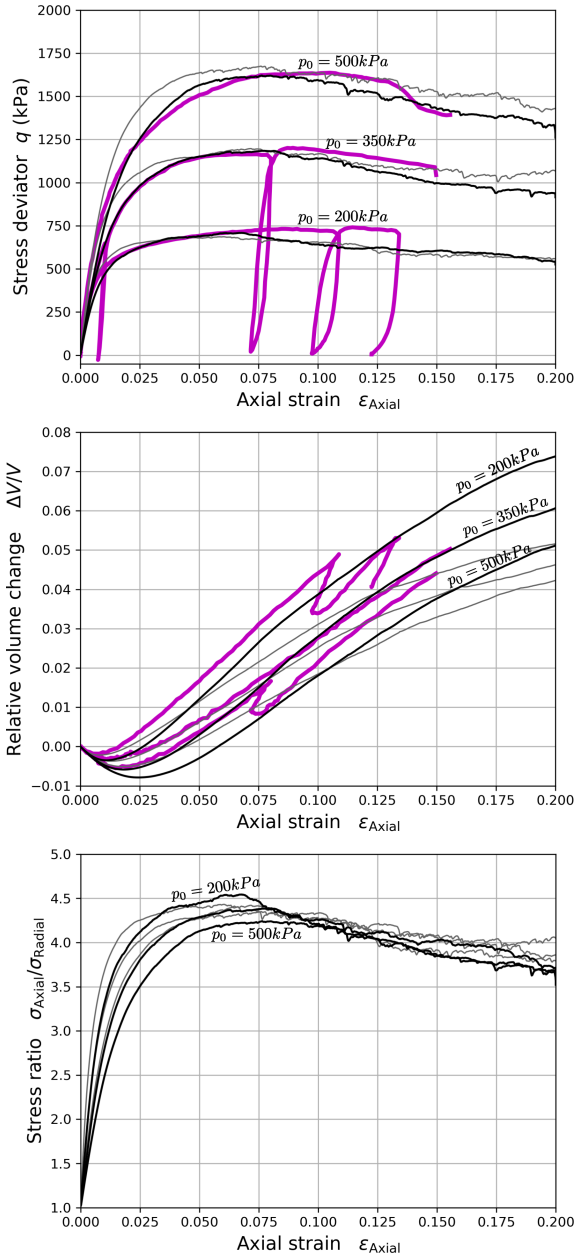

Figure 7: Calibration of the model compared to drained compressions on the dense Hostun sand from Lanier and Zitouni (1988). Experimental results are displayed in thick magenta lines (or thick gray in black and white printings), black lines correspond to the model presented in this paper, while fine gray lines show the calibration obtained with a previous model (Sibille et al., 2019) involving a constant contact friction coefficient and without tuning of the initial connectivity.

apparatus $\sigma_2 = \sigma_3 = \sigma_{\text{radial}} = p_0$). The thin grey lines in Figure 7 represent the responses simulated with a previous version of the model (Sibille et al., 2019) where the contact friction coefficient is kept constant and the initial coordination number is not calibrated. The mechanical parameters for this model were $\mu = 0.344$, $\eta_r = 0.55$ and the elastic parameters where identical to the ones in Table 1. Although the calibration of the two versions of the model are satisfying, some refinements are brought by the version presented here. The stress ratio $\sigma_{\text{axial}}/\sigma_{\text{radial}}$ depends now on the confining pressure and the peak of the stress deviator is well described whatever the confining pressure (whereas it was slightly underestimated for $p_0 = 200$ kPa and overestimated for $p_0 = 500$ kPa with the previous model). The stiffness in the hardening regime is also well described (wheresas it was overestimated in the previous version due to a high initial connectivity). Finally, the set of parameters of the model results in good reproduction of the volumetric strain rate in the phase of dilation.

Two axisymmetric drained compressions have been considered for the loose sand (even if a single compression would be enough) at the confining pressures of 200 and 300 kPa respectively (Bousquet et al., 1994; Benahmed, 2001). The maximum stress deviator is now relatively well described (compare to results shown in Figure 1). The contractancy is slightly overestimated for both tests and the stiffness in the hardening regime is better described for the test at $p_0 = 300$ kPa than for the one at $p_0 = 200$ kPa. A better description of the response of the loose sand could probably be achieved if the description of the dense sand is discarded and mechanical parameters of the model directly tuned from the loose sand tests. However, this would result in an ad hoc choice of the mechanical parameters of the model in function of the initial porosity, which is against the objectives of the paper. Furthermore, loose sand samples where created by moist tamping. This technique may lead to particular microstructures with particle aggregates and double porosity (presence of macro-pores (Benahmed et al., 2004)) which is probably not accurately simulated with the model.

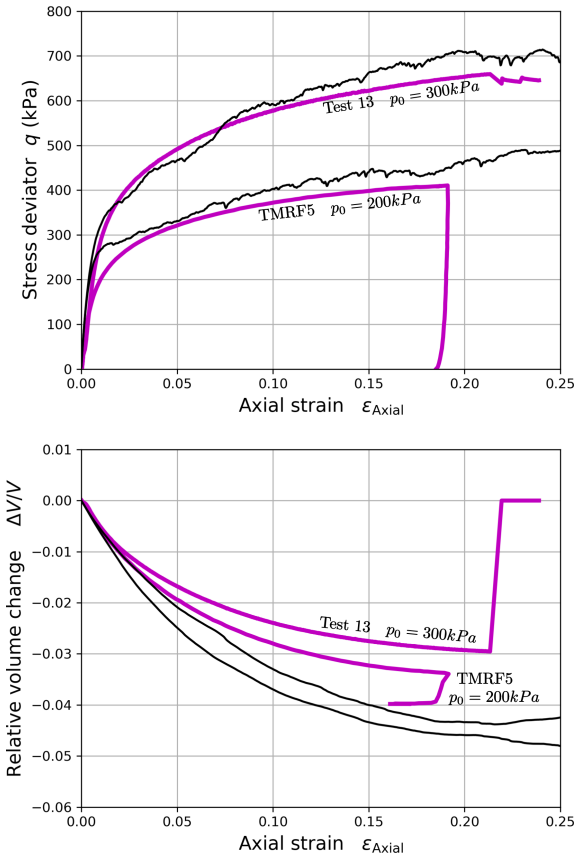

Figure 8: Calibration of the model compared to drained compressions on the loose Hostun sand; experimental results from Bousquet et al. (1994) (test 13 with $p_0 = 300$ kPa) and Benahmed (2001) (test TMRF5 with $p_0 = 200$ kPa)

5. Model validation on dense sand

The loading paths considered for the validation of the model have been chosen in such a way they are strongly different from the calibration paths, but also with respect to the availability of the experimental data. As a much wider variety of loading paths were tested on the dense Hostun sand than on a very loose one, the validation paths chosen for the dense sand differ from the ones for the loose sand.

Concerning the dense sand, two validation paths performed on the true triaxial apparatus are considered: a cyclic stress proportional loading path and a circular stress loading path. The latter path constituted one of the validation cases of the benchmark on elasto-plastic constitutive relations organized for the international workshop in Cleveland in 1987 on "Constitutive equations for granular non-cohesive soils" (Saada and Bianchini, 1988). As regards the loose sand, three kinds of validation test, performed with axisymmetric triaxial apparatuses, were considered: undrained compression paths, constant stress deviator paths, and an alternating (compression/extension) cyclic path in undrained conditions until liquefaction of the soil.

5.1. Cyclic stress proportional loading path

Stress proportional paths are performed by fixing the parameter b for a given loading path:

$$b = \frac{\sigma_2 - \sigma_3}{\sigma_1 - \sigma_3} = \text{cst.} \tag{13}$$

where σ_1, σ_2 and σ_3 are the principal stresses such that $\sigma_1 > \sigma_2 > \sigma_3$. The parameter b characterizes the intermediate stress with respect to the minor and major principal stresses. To fully define the stress state, an additional condition on the mean pressure is considered. The mean pressure is kept constant and equal to the confinement p_0 reached after the preliminary isotropic compression. Finally, tests are performed by controlling the principal strain ε_1. Consequently σ_1 is a response parameter and σ_2 and σ_3 are imposed such that:

$$\sigma_2 = \frac{1-2\,b}{b-2}\,\sigma_1 + 3\,p_0\,\frac{1-b}{2-b} \tag{14}$$

$$\sigma_3 = \frac{b+1}{b-2}\,\sigma_1 + \frac{3\,p_0}{2-b} \tag{15}$$

Experimental tests where carried out by Zitouni (1988) and two cyclic loadings are considered as presented in Figure 9:

- test SFHD72 with $b = 0.667$, leading to a three-dimensional stress state, and $p_0 = 500$ kPa;
- test SFHD216 with $b = 0$, corresponding to an axisymmetric test with respect to direction '1', and $p_0 = 200$ kPa.

For both tests, the amplitude of the first loading/unloading cycle is relatively important. Then, the amplitude of the following cycles is reduced and kept constant such that $\Delta\varepsilon_1 = 3.8\%$ for test SFHD216 and $\Delta\varepsilon_1 = 4.9\%$ for SFHD72.

The prediction of the model is globally satisfying, in particular regarding the fact that the calibration has been realized on monotonous compressions whereas cyclic responses are investigated here. For such cyclic loadings, the integration by DEM models of the loading history by the explicit description of the evolution of the soil micro-structure constitutes a strong advantage, whereas conventional phenomenological constitutive relations require the implementation of ad hoc history parameters for that purpose. In more detail, the stiffness in the compression phases of the cycles is slightly underestimated by the model, in particular for the test SFHD216. A simpler version of the model (with constant contact friction coefficient and without tuning of the initial connectivity) gaves (perhaps incidentally) a stress-strain response closer to the experimental one (Sibille et al., 2019). The simulated responses with a such simpler model are not displayed here as they stay rather close to the current one.

Besides, the predictions of the model in terms of volume change are in good agreement with the experimental measurements, and it constitutes an illustration of the consequences of the refinements brought to the definition of the

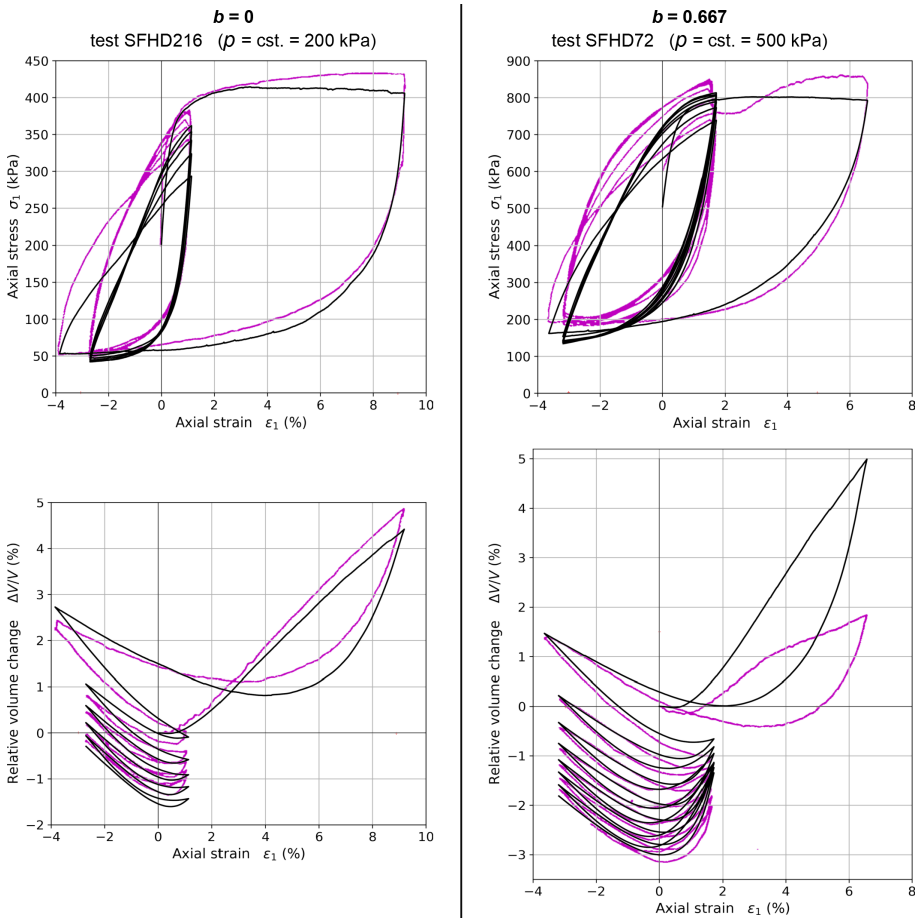

Figure 9: Validation on cyclic stress proportional loading paths with constant mean pressure on dense Hostun sand, simulated responses in black are compared with experimental results in magenta (grey).

model. The divergence between the simulated and the experimental volume changes during the first cycle of test SFHD72 is essentially due to the strain localization occurring quite early in this test (Zitouni, 1988; Lanier and Zitouni, 1988), leading the experimental observation away from what should be the intrinsic response of soil (i.e. without the bifurcation of the response into a localized mode of deformation).

5.2. Circular stress loading path

The circular stress path in the deviatoric stress plane consists in continuously changing the Lode angle while the mean pressure and the stress deviator are kept constant (Saada and Bianchini, 1988). The Lode angle φ_σ is defined from the axis s_1 (which is the projection of the σ_1 axis in the deviatoric plane) and the stress deviator intensity is represented by the second stress invariant:

$$I_{2\sigma} = \sqrt{\mathrm{tr}\,(\mathbf{s}^2)} \tag{16}$$

where $\mathbf{s}$ is the deviatoric stress tensor.

The circular stress path is performed for $p_0 = 500$ kPa and $I_{2\sigma} = 420$ kPa. Preliminary, the soil sample is isotropically compressed up to $p_0 = 500$ kPa, followed by a compression in direction '3' (i.e. $\varphi_\sigma = -120^\mathrm{o}$) with a constant mean pressure, $p = p_0$, to reach the expected value of $I_{2\sigma}$. Finally the circular stress loading is executed. It is constituted of two revolutions in the deviatoric stress plane representing a change of φ_σ from -120^o to $+600^\mathrm{o}$. Then, the mechanical state is fully stress controlled with principal stresses given by:

$$\begin{aligned} \sigma_1 &= p + \sqrt{2/3}\; I_{2\sigma}\; \cos(\varphi_\sigma) \\ \sigma_2 &= p + \sqrt{2/3}\; I_{2\sigma}\; \cos(\varphi_\sigma - 120^\mathrm{o}) \\ \sigma_3 &= p + \sqrt{2/3}\; I_{2\sigma}\; \cos(\varphi_\sigma + 120^\mathrm{o}) \end{aligned} \tag{17}$$

The representation of the strain response is split into the projection of the strain response path on the deviatoric strain plane (Bianchini et al., 1988), and the volume change (which corresponds to the strain component out of the deviatoric strain plane). The simulated response is compared in Figure 10 with the

experimental one obtained by Lanier and Zitouni (1988). The model underestimates the deformations, both in the deviatoric strain plane and in terms of volume change. This underestimation can be separated into two parts. First, the deviatoric and volumetric deformations induced during the initial comprespsion at constant mean pressure are underestimated, in particular for the volumetric component which is almost nil (quasi pure deviatoric deformation), whereas a compression in observed experimentally. Second, the deformations during the circular loading are themselves underestimated. In particular, relatively important irreversible volume reductions are observed experimentally; they are reproduced only partially by the model.

Previous predictions obtained with a simpler DEM model (with a constant contact friction coefficient, and without tuning of the initial connectivity) are represented with a thin grey line in Figure 10. The improvement of the prediction with the refined model is clear but not enough to completely fit the experimental data, even if the calibration from axisymmetric drained compressions for the dense sand is compelling (Figure 7), with in particular a good reproduction of the stiffness in the hardening regime (i.e. for a range of shear strengths mobilized during the circular stress loading).

Nevertheless, as shown during the "Cleveland workshop" (Saada and Bianchini, 1988), conventional elastoplastic constitutive relations fail to describe the response to such a loading path. The prediction given by the DEM model, even if it is not completely in agreement with the experimental results from a quantitative point of view, stays satisfying and as good as several incrementally non-linear constitutive relations (but the latter requires much more experimental tests for their calibration than such a discrete model).

6. Model validation on loose sand

6.1. Isochoric compression

Two conventional axisymmetric undrained compressions are considered, one from Benahmed (2001) (test TMRF34 with $p_0 = 200$ kPa) and another one from

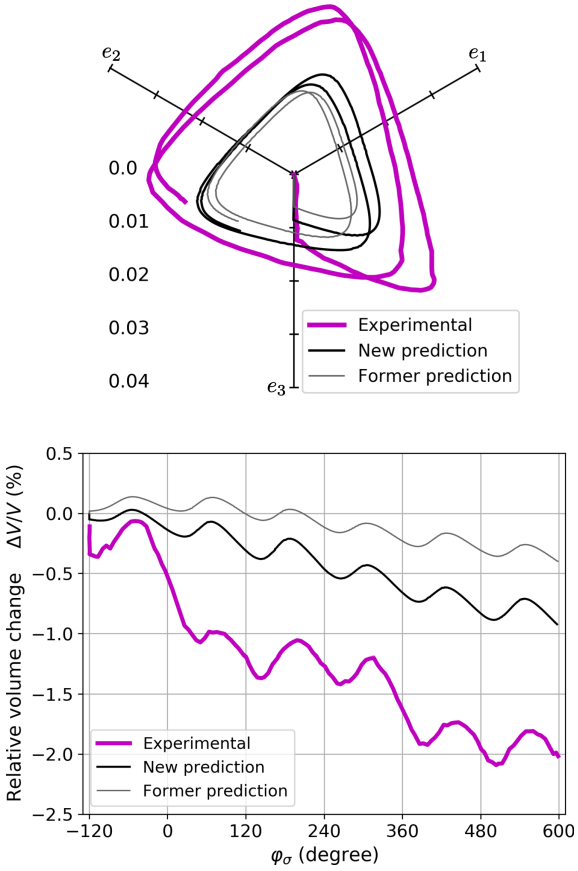

Figure 10: Validation from a circular stress loading path on dense Hostun sand: the strain response path is projected on the deviatoric strain plane (top); the relative volume change is represented in terms of the Lode angle (bottom). Black lines correspond to the model presented in this paper, while fine gray lines show the calibration obtained with a previous model (Sibille et al., 2019) involving a constant contact friction coefficient and without tuning the initial connectivity.

Bousquet et al. (1994) (test 8ND with $p_0 = 279$ kPa). Experimentally, the sand samples are saturated and compressed in undrained condition resulting in the isochoric deformation of the samples. Numerically, the water is not described and the isochoric condition is directly imposed by controlling the radial strains such that they balance the axial strain (i.e., if the sample is compressed along the direction '1' then $\varepsilon_2 = \varepsilon_3 = -\varepsilon_1/2$).

Simulated responses and experimental results are shown in Figure 11. Compare to the preliminary prediction presented in Figure 1, the description of the peak of the stress deviator has been improved and is now realistic. The q-peak is even well predicted for the test 8ND with $p_0 = 279$ kPa. For the preliminary prediction (Figure 1), the initial connectivity ($z = 4.04$ and $z_{0\mathrm{m}} = 1.57$) was lower than the one of the model currently considered ($z = 4.17$ and $z_{0\mathrm{m}} = 2.73$, Table 1). The improvement may result from the tuning of the initial coordination number and the general increase of the contact friction coefficient when the effective mean pressure decreases.

Nevertheless, once the q-peak is reached, the model still presents a more unstable response than the sand samples, resulting in a complete liquefaction (vanishing of the effective stresses) for a low axial deformation, whereas experimentally the liquefaction is rather partial and requires a larger deformation of the samples. In the real sand, the rotation of angular shaped particles, or particles with anisotropic shapes, can have some direct kinematics effects as a local tendency to dilation, or at least as a particle interlocking under the global isochoric constraint, helping to stabilize the mechanical response. The numerical model involves a rolling resistance at contacts but with spherical particles; this may fail to completely described such a local mechanism, particularly from a kinematics point of view.

6.2. q-constant path

Constant stress deviator loading path consists in decreasing the effective mean pressure p while the stress deviator q is kept constant from a stress state reached after a preliminary drained compression. Two experimental tests per-

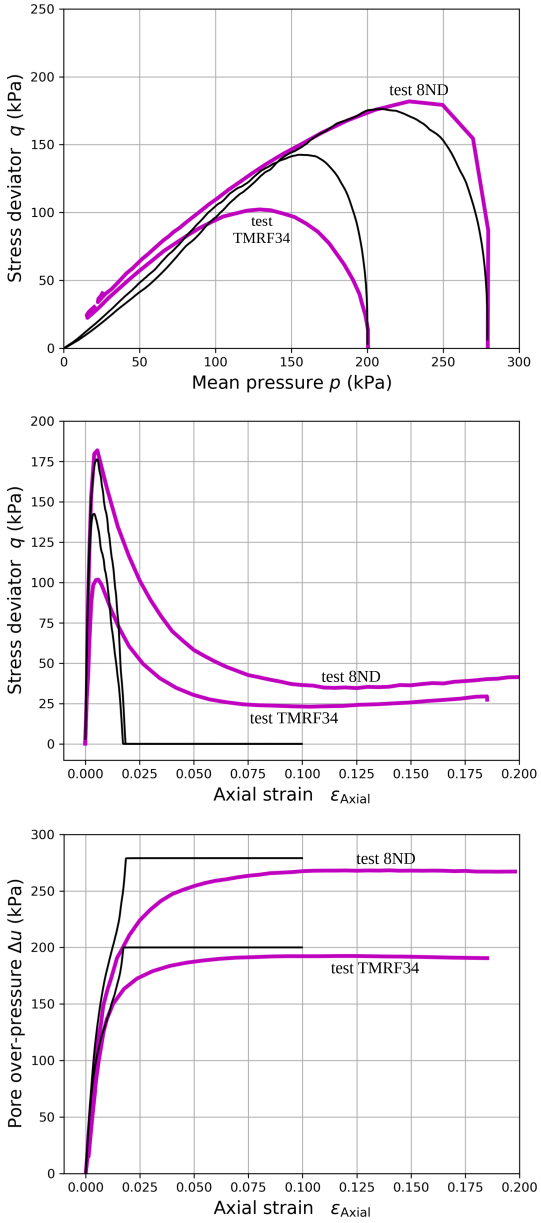

Figure 11: Validation on undrained axisymmetric compressions on loose Hostun sand, comparison with experimental tests 8ND with $p_0 = 279$ kPa (Bousquet et al., 1994) and TMRF34 with $p_0 = 200$ kPa (Benahmed, 2001).

formed from an initial confinement $p_0 = 300$ kPa, and conducted by Daouadji et al. (2011), are considered. For test CSD1, the stress deviator reached after the initial drained compression is $q = 119$ kPa. The subsequent q-constant path is realized by slowly increasing the pore pressure while the total stresses applied to the sand sample are kept constant. For test CSD2, the initial drained compression was stopped at $q = 54$ kPa, and the q-constant path was achieved by decreasing the total stresses ($\dot{\sigma}_{\text{axial}} = \dot{\sigma}_{\text{radial}} < 0$), while the pore pressure is maintained constant.

Numerically, the water phase is not described (as for the isochoric tests) and the q-constant loading is prescribed similarly to the test CSD2, by imposing after the preliminary compression:

$$\dot{\sigma}_1 = \dot{\sigma}_2 = \dot{\sigma}_3 = c \tag{18}$$

where c is a negative constant. Then $\dot{p} = c$ and $\dot{q} = 0$.

Numerical predictions are compared with the experimental results in Figure 12. There is a lack of repeatability of the experimental response concerning the deformations induced by the initial drained compression. However, it is clear that both axial shortening and volume reduction are underestimated by the model during this initial drained compression. It concerns a low deformation range only ($\varepsilon_{\text{axial}} < 0.5$ %) and this is mainly a matter of elastic properties. Besides, it is important to keep in mind that the operators and the testing equipments for these tests are different from the ones involved for the drained compression tests used for the calibration (Figures 7 and 8). Moreover, the general configuration of the numerical model (parallelepipedic granular assembly with periodic limit conditions) is different from the experimental tests (cylindrical sand samples inside a latex membrane and in between bottom and top plates). Consequently, the identification of the origin of the difference for such low deformations is not straightforward.

Concerning the q-constant loading itself, the strong dilation observed at the beginning of the loading is now reproduced by the model, whereas it was lacking in the preliminary prediction (Figure 1). However this dilation is still underes-

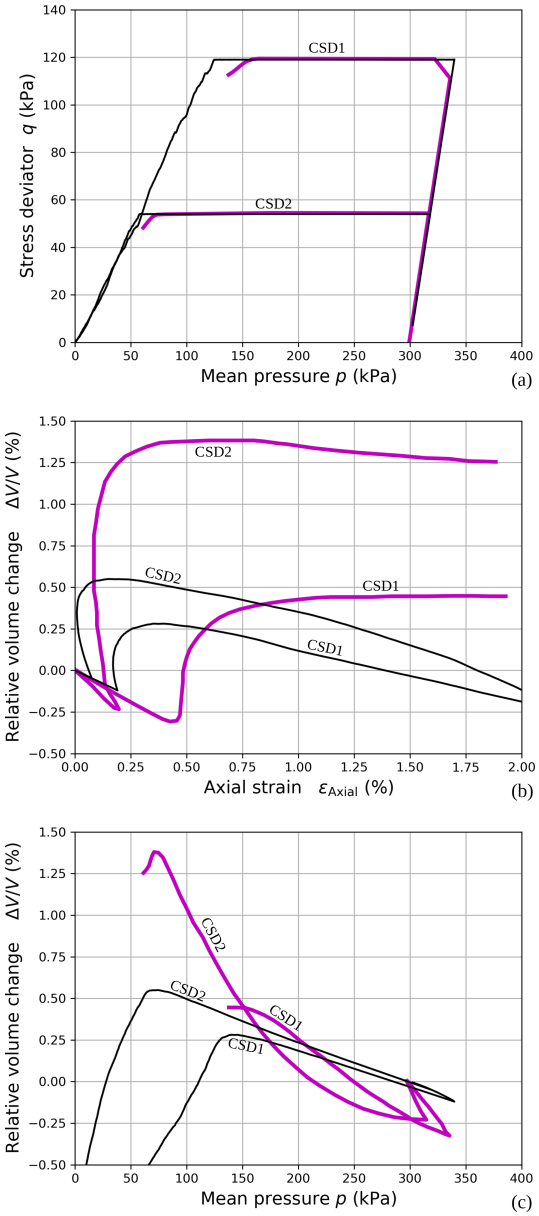

Figure 12: Validation on constant stress deviator loading paths on loose Hostun sand, comparison with experimental tests CSD1 with $q = 119$ kPa, and CSD2 with $q = 54$ kPa from Daouadji et al. (2011).

timated, in particular for the test CSD2. Once the dilation peak is reached, the model predicts a collapse of the sample which is more sudden (in terms of axial strain as shown in Figure 12b) than what is observed experimentally (even if few experimental data is available after the dilatation peak).

Here again, a more dilatant response is expected for stronger contact friction coefficients (Aboul Hosn et al., 2017) and the introduction of an increasing contact friction coefficient while the normal contact forces lower (and so does the mean pressure) promotes a dilatant response along the q-constant path. However, this mechanisms is not sufficient to completely recover quantitatively the experimental observations.

6.3. Alternating undrained cyclic loading

Undrained cyclic loadings performed by Benahmed (2001) on saturated sand samples with a conventional axisymmetric triaxial cell are considered. The loadings are performed by controlling the stress deviator which is imposed to alternate cyclically with an amplitude q_{cyc} between compression (up to $q = q_{\text{cyc}}$), and extension (down to $q = -q_{\text{cyc}}$) around a nil stress deviator state. Experimentally, the isochoric condition is maintained by closing the sample drainage, whereas numerically the isochoric condition is reached by imposing $\varepsilon_2 = \varepsilon_3 = -\varepsilon_1/2$.

Simulated and experimental responses are displayed in Figure 13. As the soil is sufficiently loose and the cycle amplitude q_{cyc} sufficiently large, the loading leads to the total liquefaction of the sample (vanishing of the effective stresses) for both simulated and experimental responses. The main difference between the model and the experience is the response path followed during the extension phase of the cycles. This is particularly visible for the first cycle: experimentally, the pore overpressure generated during the compression phase of the cycle is only partially vanished during the subsequent extension phase and no negative overpressure is developed. Numerically, a much more reversible response is observed, with a reduction of the overpressure (previously generated during

the compression phase) down to a negative value during the extension phase (but with a magnitude lower than in the compression phase). This different behaviour results experimentally in a faster growth of the pore overpressure with cycles and a faster decrease of the mean effective pressure (always with respect to the number of cycles), particularly during the extension phase of the cycles. Consequently, the number N of cycles to reach the liquefaction is higher for the simulated response ($N = 31$) than for the experience ($N = 5$).

An element in the global constitution of the model is probably missing to describe accurately this different behaviour in compression and in extension. It may be related to the anisotropy of the fabric of the sand samples (built by moist tamping), while contact orientations in numerical samples are rather isotropic. We attempted to build anisotropic granular assemblies, but the effect on the simulated response to such alternating cyclic loadings was far from sufficient to close the gap with the experimental data. The inter-particle contact law with a normal stiffness identical in compression and decompression may also be incriminated, the contact between sand particles being possibly slightly damaged at each loading.

However, in all cases, the number of cycles to reach the liquefaction seems to be very sensitive to the initial state. Experimentally, for the sand density considered here, it has been shown that N may change with a factor from 0.2 to 2.7 depending on q_{cyc} (Benahmed, 2001) (the factor decreasing when q_{cyc} increases). Numerically, Figure 14 gives an indication of the repeatability of the simulated responses for six simulations performed from different random generations of the initial positions of the particles. N ranges from 22 to 43, representing a maximum factor of 2. Furthermore, the initiation threshold of the instability in terms of effective mean pressure and pore overpressure is rather well reproducible experimentally (Benahmed, 2001), even if, for the same tests, the number of cycles to reach the liquefaction is not. Similarly, the numerical model gives here a good prediction of the initiation threshold of the instability, occurring numerically and experimentally at about $p = 100$ kPa and $\Delta u = 100$ kPa

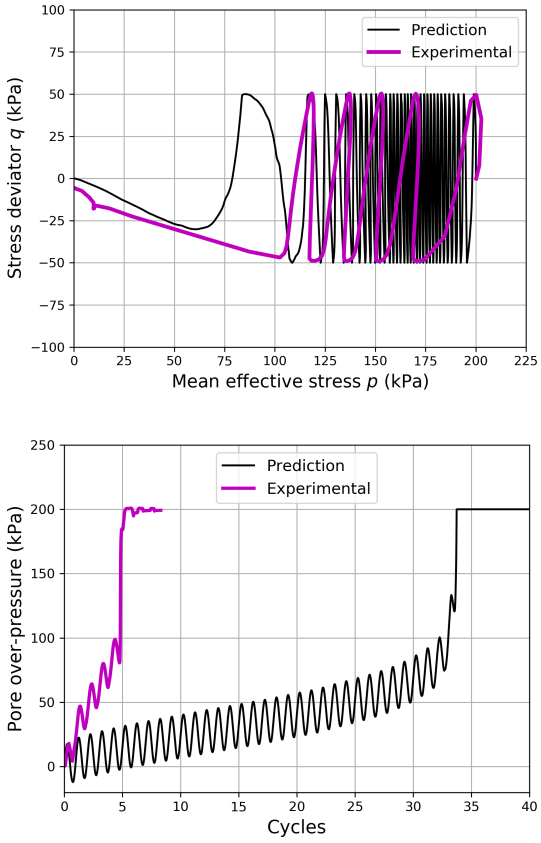

Figure 13: Cyclic liquefaction test on loose Hostun sand: predicted response with the discrete model and experimental results from Benahmed (2001).

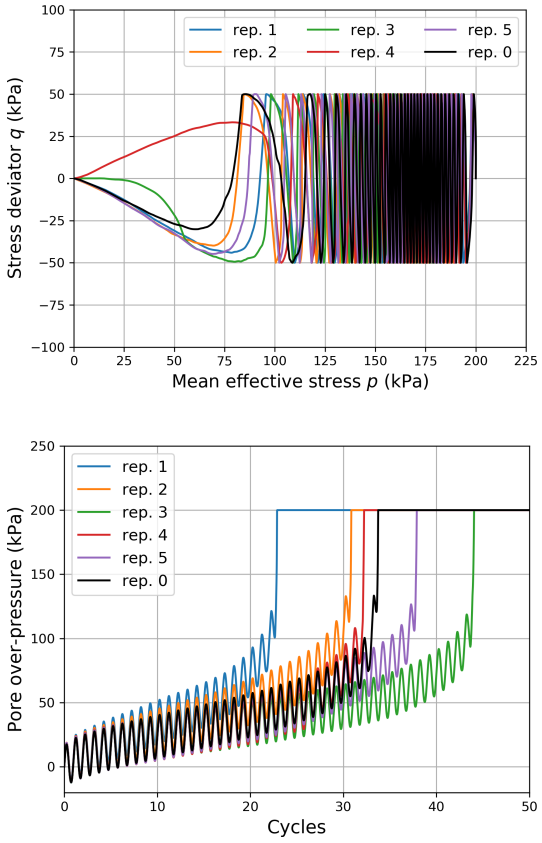

Figure 14: Repeatability of the simulated response to an alternating undrained cyclic loading on the loose Hostun; each simulation is performed from a different random draw of initial particle positions.

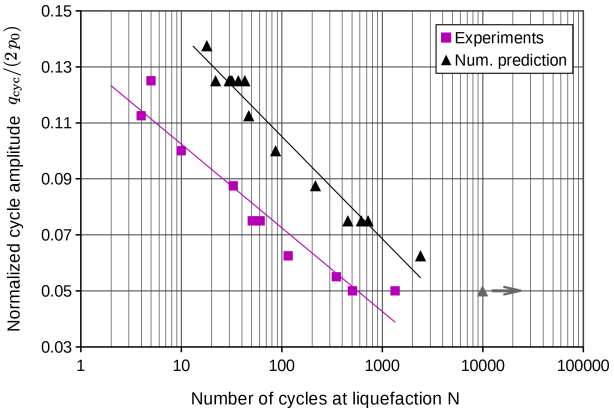

Figure 15: Experimental and predicted cyclic shear strength of Hostun sand RF at a relative density $D_{\mathrm{r}} = 0.1$; experimental data after Benahmed (2001).

(Figure 13).

Although the number N of cycles to reach liquefaction is a sensitive parameter, his dependence on the cycle amplitude can be interestingly investigated, as q_{cyc} can affect the number of cycles in a wide range of several decades. Experimental and simulated results of the cyclic shear strength of Hostun sand at $D_{\mathrm{r}} = 0.1$ are presented in Figure 15. The normalized cycle amplitude $(q_{cyc}/(2p_0))$ is plotted with respect to N. The model overestimates the number of cycles to initiate liquefaction by a factor of 10, however the trend is rather fairly reproduced: the slopes of the linear regressions (in the semi-logarithmic diagram) are equal to -0.0299 and -0.0365 for the experimental and simulated data respectively (the grey triangle symbol corresponding to the lowest cycle amplitude has not been considered for the regression, as discussed further). This result has to be considered relatively to the fact that no calibration of the model has been done from cyclic tests. The remaining shift between experimental and numerical point can be attributed to the constitutive model itself, but the difference in the boundary conditions could be also incriminated (cylindrical sand sample inside a rubber membrane experimentally, periodic parallelepipedic cell for the model).

Concerning the lowest tested cycle amplitude ($q_{cyc}/(2p_0) = 0.05$), the model did not predict liquefaction after the simulation of 10,000 cycles (grey triangle symbol in Figure 15), and presents instead an accommodation of the simulated response. The liquefaction may be simulated for an higher number of cycles but, even if it occurs, it will differ importantly from the number of cycles identified experimentally (roughly in the range 500 to 1,000 cycles) and the simulation has not been pursued beyond. As found numerically, the number of cycles at liquefaction necessarily diverges below a given cycle amplitude since no liquefaction is expected for a vanishing amplitude of the cycles. Experimentally, accommodation without liquefaction was observed for $q_{cyc}/(2p_0) = 0.025$. Consequently, the threshold to trigger the cyclic liquefaction should be in between values of normalized cycle amplitude of 0.05 and 0.025, although it has not be been investigated specifically.

In conclusion, the non negligible overestimation of the number of cycles to reach the liquefaction shows that the limits of the model are approached in such conditions. However, it is worth noting that the obtained general trend is consistent. Moreover, the use of such a model can be interesting to get an estimation of the undrained cyclic shear strength of the soil when only results from monotonic compressions are available (which is generally not reachable from phenomenological constitutive relations).

7. Concluding discussion

Constitutive responses of Hostun sand RF in both dense and loose state have been simulated with a discrete element model. The model is made of spherical particles with a contact law involving an inter-particle rolling resistance and a tangential friction coefficient dependent on the contact normal stress. The six mechanical parameters of the model (3 elastic parameters and 3 plastic parameters) were calibrated from drained monotonous triaxial compressions performed on an initially dense and loose sand. The mechanical parameters of the contact

law are considered intrinsic to the sand grains, and different initial states of the sand are represented by tuning both the initial porosity and connectivity of the numerical granular assembly, while contact mechanical parameters are kept constant.

The proposed calibration process focuses mainly on the plastic parameters of the model (two tangential friction coefficients plus one rolling friction coefficient), as the response of the model relies mainly on these parameters if the elastic parameters (normal, tangential and rolling stiffnesses) are chosen close to the rigid grain limit (i.e. sufficiently high to avoid interplay with the plastic parameters). Then, the initial micro-structure of the numerical assembly is an essential ingredient, determining in particular the simulated response for reduced deformation, in the pre-failure regime (for example before the deviatoric stress peak for a drained compression). In this context, the control of the initial porosity of the numerical sample only is not enough to correctly describe the intrinsic soil response for moderate deformations. The tuning of the initial connectivity improve the calibration and the prediction of the model, in particular in the hardening regime of the response.

Regarding the benefit of such a model with respect to its prediction capabilities, the improvements brought by the tangential friction coefficient function of the normal contact stress, and the control of the initial connectivity, are really significant is the case of the loose sand, in particular when subjected to isochoric and constant stress deviator loading paths. Without such enrichment, the simulated response may diverge not only quantitatively but also qualitatively from the constitutive response measured experimentally. Nevertheless, some parts of the constitutive response are still not completely captured. In undrained conditions, so when the sample is kinematically constrained, the numerical loose sample is more unstable than the real one. For the q-constant path, which is fully stress controlled, the induce dilatation is underestimated. Finally, the number of cycles to reach liquefaction is systematically overestimated by the model.

In the case of the dense sand, these enhance contact law and preparation methodology lead to a better calibration of the model on drained compressions, with respect to a simpler model with a constant tangential friction coefficient and a control of the initial porosity uniquely. However, predictions on the considered loading paths (cyclic stress proportional and circular stress loading paths) are only slightly improved with respect to the cost brought by the more complex model calibration and control of the initial state. The simpler model version (Sibille et al., 2019) may be more attractive due its easier implementation and still really good prediction capabilities in these conditions.

Hence, this work highlights the difficulty to define and calibrate such a discrete model in order to reach an accurate description of the constitutive response of a given soil over a wide range of initial densities (here for a relative density from 0.1 to 1.0), as suggested in Gu et al. (2020) but for a narrower range of initial densities.

Despite the above limitations, the prediction capabilities of the discrete model on complex loading paths (true 3D loading paths, with rotation of principal stress axises, loading/unloading cycles, ...), considered relatively to the mechanical tests necessary for the calibration (few monotonous compressions), are above what can be expected from conventional elasto-plastic relations (Saada and Bianchini, 1988). The reduce number of calibration tests and their relative simplicity (no need of cyclic or extension calibration tests for instance) constitutes an advantage in an engineering context where a thorough mechanical characterization of all soil layers may be too demanding.

References

Aboul Hosn, R., Sibille, L., Benahmed, N., Chareyre, B., 2017. Discrete numerical modeling of loose soil with spherical particles and interparticle rolling friction. Granular matter 19. doi:10.1007/s10035-016-0687-0.

Bardet, J., 1994. Numerical simulations of the incremental responses of idealized granular materials. International Journal of Plasticity 10, 879–908.

Barton, N., Kjaernsli, B., 1981. Shear strength of rockfill. Journal of the Geotechnical Engineering Division 107, 16374. doi:10.1061/AJGEB6.0001167.

Belheine, N., Plassiard, J.P., Donzé, F.V., Darve, F., Seridi, A., 2009. Numerical simulation of drained triaxial test using 3d discrete element modeling. Computers and Geotechnics 36, 320–331. doi:0.1016/j.compgeo.2008.02.003.

Benahmed, N., 2001. Comportement mécanique d'un sable sous cisaillement monotone et cyclique: application aux phénomènes de liquéfaction et de mobilité cyclique. Ph.D. thesis. Ecole nationale des ponts et chaussées.

Benahmed, N., Canou, J., Dupla, J., 2004. Structure initiale et propriétés de liquéfaction statique d'un sable. Comptes Rendus Mécanique 332, 887 – 894. doi:https://doi.org/10.1016/j.crme.2004.07.009.

Bianchini, G., Puccini, P., Saada, A., 1988. Test results, in: Saada, A., Bianchini, G. (Eds.), Constitutive equations for granular non-cohesive soils - Proceedings of the international workshop on constitutive equations for granular non-cohesive soils, Balkema, Rotterdam, 22-24 July 1987, Cleveland. pp. 89–97.

Bousquet, H., Djeddid, M., Khazar, E., Flavigny, E., Hajd-Sadok, M., Lanier, J., Lefebvre, P., Meghachou, M., Zitouni, Z., 1994. Compilation des essais triaxiaux de révolution sur le sable d'Hostun RF. Technical Report. Institut de mécanique de Grenoble.

Chu, J., 1995. An experimental examination of the critical state and other similar concepts for granular soils. Canadian Geotechnical Journal 32, 1065–1075.

Combe, G., Roux, J., 2011. Discrete-Element Modeling of Granular Materials. iSTE-Wiley. chapter 6: Construction of Granular Assemblies under Static Loading.

Cundall, P., Strack, O., 1979. A discrete numerical model for granular assemblies. Geotechnique 29, 47–65.

Daouadji, A., Darve, F., Al Gali, H., Hicher, P., Laouafa, F., Lignon, S., Nicot, F., Nova, R., Pinheiro, M., Prunier, F., Sibille, L., Wan, R., 2011. Diffuse failure in geomaterials: Experiments, theory and modelling. Int. J. Numer. Anal. Meth. Geomech. 35, 1731–1773.

Darve, F., Dendani, H., 1988. An incrementally non-linear constitutive relation and its predictions, in: Saada, A., Bianchini, G. (Eds.), Constitutive equations for granular non-cohesive soils - Proceedings of the international workshop on constitutive equations for granular non-cohesive soils, Balkema, Rotterdam, 22-24 July 1987, Cleveland. pp. 237–254.

Darve, F., Flavigny, E., Meghachou, M., 1995. Yield surfaces and principle of superposition revisited by incrementally non-linear constitutive relations. International Journal of Plasticity 11, 927–948.

Flavigny, E., Desrues, J., B., P., 1990. Le sable d'hostun rf. Revue Française de géotechnique , 67–70.

Gu, X., Zhang, J., Huang, X., 2020. Dem analysis of monotonic and cyclic behaviors of sand based on critical state soil mechanics framework. Computers and Geotechnics 128, 103787. doi:https://doi.org/10.1016/j.compgeo.2020.103787.

Hassan, S., El Shamy, U., 2019. Dem simulations of the seismic response of granular slopes. Computers and Geotechnics 112, 230–244.

Hazzar, L., Nuth, M., Chekired, M., 2020. Dem simulation of drained triaxial tests for glass-beads. Powder Technology 364, 123–134. doi:https://doi.org/10.1016/j.powtec.2019.09.095.

Iwashita, K., Oda, M., 2000. Micro-deformation mechanism of shear banding process based on modified distinct element method. Powder Technology 109, 192–205.

Jiang, M., Zhang, A., Li, T., 2019. Distinct element analysis of the microstructure evolution in granular soils under cyclic loading. Granular Matter 21, 39. doi:https://doi.org/10.1007/s10035-019-0892-8.

Karapiperis, K., Harmon, J., Ando, E., Viggiani, G., Andrade, J., 2020. Investigating the incremental behavior of granular materials with the level-set discrete element method. Journal of the Mechanics and Physics of Solids 144, 104103. doi:10.1016/j.jmps.2020.104103.

Kawamoto, R., Ando, E., Viggiani, C., Andrade, J., 2018. All you need is shape: Predicting shear banding in sand with ls-dem. Journal of the Mechanics and Physics of Solids 111, 375–392. doi:10.1016/j.jmps.2017.10.003.

Lancelot, L., Shahrour, I., Al Mahmoud, M., 2006. Failure and dilatancy properties of sand at relatively low stresses. Journal of Engineering Mechanics 132, 1396–1399.

Lanier, J., Zitouni, Z., 1988. Development of a data base using the grenoble true triaxial apparatus, in: Saada, A., Bianchini, G. (Eds.), Constitutive equations for granular non-cohesive soils - Proceedings of the international workshop on constitutive equations for granular non-cohesive soils, Balkema, Rotterdam, 22-24 July 1987, Cleveland. pp. 47–58.

Lee, S., Hashash, Y., Nezami, E., 2012. Simulation of triaxial compression tests with polyhedral discrete elements. Computers and Geotechnics 43, 92–100. doi:10.1016/j.compgeo.2012.02.011.

Li, L., Wu, W., El Naggar, M., Mei G., L.R., 2019. Dem analysis of the sand plug behavior during the installation process of open-ended pile. Computers and Geotechnics 109, 23–33. doi:10.1016/j.compgeo.2019.01.014.

Maksimovic, M., 1989. Nonlinear failure envelope for soils. Journal of Geotechnical Engineering 115, 581–586. doi:10.1061/(ASCE)0733-9410(1989)115:4(581).

Martin, E., Thornton, C., Utili, S., 2020. Micromechanical investigation of liquefaction of granular media by cyclic 3d dem tests. Géotechnique 70, 906–915. doi:10.1680/jgeot.18.P.267.

Oda, M., Iwashita, K., 2000. Study on couple stress and shear band development in granular media based on numerical simulation analyses. International Journal of Engineering Science 38, 1713 – 1740. doi:10.1016/S0020-7225(99)00132-9.

Plassiard, J., Belheine, N., Donzé, F., 2009. A spherical discrete element model: calibration procedure and incremental response. Granular Matter 11, 293–306. doi:10.1007/s10035-009-0130-x.

Popov, V., 2017. Contact Mechanics and Friction. Springer. chapter 10 Coulomb's Law of Friction. pp. 151–172.

Popova, E., Popov, V., 2015. The research works of coulomb and amontons and generalized laws of friction. Friction 3, 183–190. doi:10.1007/s40544-015-0074-6.

Quezada, J., Breul, P., Saussine, G., Radjai, F., 2014. Penetration test in coarse granular material using contact dynamics method. Computers and Geotechnics 55, 248–253. doi:10.1016/j.compgeo.2013.09.006.

Rajaï, F., Wolf, D., Jean, M., Moreau, J., 1998. Bimodal character of stress transmission in granular packings. Physical Review Letters 80, 61–64.

Rorato, R., Arroyo, M., Gens, A., Andò, E., Viggiani, G., 2021. Image-based calibration of rolling resistance in discrete element models of sand. Computers and Geotechnics 131, 103929. doi:https://doi.org/10.1016/j.compgeo.2020.103929.

Roux, J., Chevoir, F., 2005. Discrete numerical simulation and the mechanical behavior of granular materials. Bulletin des laboratoires des ponts et chaussées 254, 109–138.

Roux, J., Combe, G., 2010. How granular materials deform in quasistatic conditions, in: J. D. Goddard, J. T. Jenkins, P.G. (Ed.), IUTAM-ISIMM Symposium on Mathematical Modeling and Physical Instances of Granular Flow, AIP Conference Proceedings (vol. 1227). p. 260.

Saada, A., Bianchini, G., 1988. Constitutive equations for granular non-cohesive soils - Proceedings of the international workshop on constitutive equations for granular non-cohesive soils. Balkema, Rotterdam, 22-24 July 1987, Cleveland.

Shire, T., O'Sullivan, C., Hanley, K., Fannin, R., 2014. Fabric and effective stress distribution in internally unstable soils. Journal of Geotechnical and Geoenvironmental Engineering 140, 04014072. doi:10.1061/(ASCE)GT.1943-5606.0001184.

Sibille, L., Hadda, N., Nicot, N., Tordesillas, A., Darve, F., 2015. Granular plasticity, a contribution from discrete mechanics. Journal of the Mechanics and Physics of Solids 75, 119–139. doi:10.1016/j.jmps.2014.09.010.

Sibille, L., Villard, P., Darve, F., Aboul Hosn, R., 2019. Quantitative prediction of discrete element models on complex loading paths. International Journal for Numerical and Analytical Methods in Geomechanics 43, 858–887. doi:10.1002/nag.2911.

Smilauer, V., 2015. Yade Documentation 2nd ed. The Yade Project. URL: http://yade-dem.org/doc/, doi:10.5281/zenodo.34073.

Suhr, B., Six, K., 2017. Friction phenomena and their impact on the shear behaviour of granular material. Computational Particle Mechanics 4, 23–34. doi:10.1007/s40571-016-0119-2.

Tatsuoka, F., Goto, S., Sakamoto, M., 1986. Effects of some factors on strength and deformation characteristics of sand at low pressures. Soils and Foundations 26, 105–114.

Thornton, C., 2000. Numerical simulations of deviatoric shear deformation of granular media. Géotechnique 50, 43–53. doi:10.1680/geot.2000.50.1.43.

Villard, P., Chareyre, B., 2004. Design methods for geosynthetic anchor trenches on the basis of true scale experiments and discrete element modelling. Canadian Geotechnical Journal 41, 1193–1205. doi:10.1139/t04-063.

Villard, P., Huckert, A., Briançon, L., 2016. Load transfer mechanisms in geotextile-reinforced embankments overlying voids: Numerical approach and design. Geotextiles and Geomembranes 44, 381–395. doi:10.1016/j.geotexmem.2016.01.007.

Widulinski, L., Kozicki, J., Tejchman, J., 2009. Numerical simulations of triaxial test with sand using dem. Archives of Hydro-Engineering and Environmental Mechanics 56, 149–172.

Wu, W., 1990. The behaviour of very loose sand in the triaxial compression test. Canadian Geotechnical Journal 27, 159–163.

Zitouni, Z., 1988. Comportement tridimensionnel des sables. Ph.D. thesis. Université Joseph Fourier - Grenoble 1. Grenoble, France.